MATERIALS CHEMISTRY FRONTIERS

RESEARCH ARTICLE

View Article Online
View Journal | View Issue

Cite this: *Mater. Chem. Front.*, 2025, **9**, 3559

Branched siloxane axial substituents outperform linear analogues in a model silicon phthalocyanine-based organic thin film transistor

Nicolas Ledos, [ab] Halynne R. Lamontagne, [ab] Joseph G. Manion, [a] Jaclyn L. Brusso *[b] and Benoît H. Lessard *[ac]

The rational design of organic semiconductors (OSCs) necessitates a deep understanding of structure–property relationships, where side chain engineering is as critical as the conjugated core itself. While hybrid organic–inorganic siloxane side chains have shown great promise for optimizing morphology and charge transport, a systematic study to deconvolute the impact of their architecture in a simplified molecular system has yet to be conducted. To address this, we employ silicon phthalocyanine (SiPc) as an accessible, symmetrical platform to isolate the effects of siloxane substituents. We report the synthesis of a series of axially-substituted siloxane-SiPc derivatives where the length and branching of the siloxane chains are systematically varied. These molecules are integrated into organic thin-film transistors (OTFTs) and comprehensively characterized using atomic force microscopy (AFM), X-ray diffraction (XRD), and ultraviolet photoelectron spectroscopy (UPS). Our results establish clear design rules, revealing that branched siloxane chains are vastly superior to linear analogs. The best derivative molecule, bearing branched 1,1,1,3,5,5,5-heptamethyltrisiloxane chains, achieves a high average hole mobility exceeding 1 $cm^2 V^{-1} s^{-1}$, a performance nearly three orders of magnitude greater than its linear counterpart. This improvement is attributed to the ability of the branched chains to promote a uniform crystalline texture, smooth morphology, and tighter π-stacking. This work provides fundamental insights and practical guidelines for implementing siloxane chains in next-generation, high-performance organic electronic devices.

Received 5th October 2025,
Accepted 10th November 2025

DOI: 10.1039/d5qm00722d

rsc.li/frontiers-materials

Introduction

The pursuit of high-performance organic semiconductors (OSCs) for applications in flexible electronics, photovoltaics, and displays has increasingly focused on the critical role of side chain engineering. While the conjugated backbone dictates fundamental electronic properties such as the bandgap and charge transport characteristics, the appended side chains govern crucial morphological and physical processes, including molecular packing, thin-film crystallinity, and solubility. Among the plethora of side chain functionalities, hybrid organic-inorganic siloxane-based chains have emerged as particularly promising.[1,2] Their unique combination of high flexibility, low polarizability, and pronounced hydrophobicity offers a powerful toolset to modulate intermolecular interactions and self-assembly without disrupting the electronic structure of the core.[3] Thus far, their use has mainly been explored in designing new, efficient conjugated polymers for organic thin-film transistor (OTFT)[4–6] and organic photovoltaic (OPV)[7–9] applications. Recent studies have focused on the impact of siloxane unit position, the best ratio of alkyls to siloxane chains,[10] the type of linker,[7,11–13] and the size of the alkyl spacer.[14] As well, a few studies have been conducted to identify the optimal length and isomer of the siloxane side chain;[3,15–17] however, these studies were only conducted on conjugated polymers, in which many parameters are simultaneously modulated, making it challenging to derive clear design rules. Although siloxanes have also been successfully incorporated into small molecules,[9,18,19] systems with inherently fewer variables, a systematic study to identify the optimal siloxane architecture (*e.g.*, length, branching) in this context remains absent.

To address this knowledge gap and deconvolute these structure–property relationships, we turned to a uniquely elegant molecular platform: silicon phthalocyanine (SiPc). SiPcs are a class of organic semiconductors that display efficient mobilities (μ) and

[a] *Department of Chemical and Biological Engineering, University of Ottawa, 161 Louis Pasteur, Ottawa, Ontario K1N 6N5, Canada. E-mail: benoit.lessard@uottawa.ca*
[b] *Department of Chemistry and Biomolecular Sciences, University of Ottawa, 150 Louis Pasteur, Ottawa, ON, K1N 6N5, Canada. E-mail: jbrusso@uottawa.ca*
[c] *School of Electrical Engineering and Computer Science, University of Ottawa, 800 King Edward Ave. Ottawa, Ontario K1N 6N5, Canada*

are particularly interesting for establishing structure–property relationships due to their high versatility and facile synthesis.[20–24] Over the years, our groups have explored many aspects of SiPc based OTFTs: contact materials,[25] interface or dielectric engineering,[26–30] processing conditions,[31,32] peripheral fluorination and more.[33,34] We recently developed high-performance OTFTs based on a SiPc core axially substituted with siloxane chains (^{iso}**(Si$_3$O)$_2$SiPc**).[35] This molecule exhibits exceptional μ_h, attributed to its highly uniform crystalline texture. Its topology is singular: the siloxane moiety is directly grafted onto the central silicon atom of the π-conjugated system, eliminating any ancillary linkers and resulting in a model architecture of minimal complexity. This reduction to a highly symmetrical π-core and the siloxane chains makes siloxane-SiPcs ideal candidates for a systematic investigation into the role of siloxane substituents.

In this work, we report a new synthesis pathway to access a series of four siloxane-SiPc derivatives featuring systematically varied siloxane chain length and branching. We integrated these materials into OTFTs and evaluated their semiconducting properties through experimental electrical characterization. The effects of siloxane structure and post-deposition thermal annealing on thin-film morphology and molecular packing were elucidated using atomic force microscopy (AFM) and both 1D and 2D X-ray diffraction (XRD). Our comprehensive study establishes clear design rules, revealing that branched siloxane chains are vastly superior to their linear counterparts for OTFT applications. We demonstrate that this superiority stems from the ability of branched chains to promote the formation of highly crystalline films with a uniform crystalline texture and smooth morphology, which are critical for efficient charge transport. This work provides fundamental insights into siloxane side chain engineering, offering a strategic guide for their implementation in next-generation organic electronic devices.

Experimental section

Materials

All solvents used for synthesis and device fabrication were ACS grade and were used without any further purification. All silanes were purchased from Sigma-Aldrich and used as received. Silicon phthalocyanine dichloride,[36] 1,1,3,3,3-pentamethyldisiloxan-1-ol,[37] 1,1,3,3,5,5,5-heptamethyltrisiloxan-1-ol,[37] 1,1,1,3,5,5,5-heptamethyltrisiloxan-3-ol,[37] and tris(trimethylsiloxy)silanol,[38] were synthesized using previously reported protocols.

Synthetic procedures

(Si$_2$O)$_2$SiPc. Silicon phthalocyanine dichloride (1.00 g, 1.64 mmol) was added into a two-neck round bottom flask equipped with a reflux condenser and three nitrogen-vacuum cycles were performed. The flask was subsequently filled with 80 mL of dry toluene, triethylamine (8 mL, 57.4 mmol) and 1,1,3,3,3-pentamethyldisiloxan-1-ol (0.81 g, 4.9 mmol) and the resulting mixture was sparged with N_2 for 10 minutes before heating to reflux overnight. After cooling to rt., the mixture was filtered on a fine frit and the remaining solids were rinsed with dichloromethane (DCM) until the solvent came out clear. After removing the solvent under vacuum, the product was purified by column chromatography on silica gel (eluent: Hexane 100% to DCM/Hexane = 1/3), affording **(Si$_2$O)$_2$SiPc** as a blue crystalline solid in 54% yield (768 mg). ^{1}H NMR (600 MHz, $CDCl_3$) δ 9.73–9.57 (m, 8H), 8.40–8.25 (m, 8H), −1.22 (s, 18H), −2.87 (s, 12H). ^{13}C NMR (151 MHz, $CDCl_3$) δ 148.86, 136.31, 130.71, 123.67, 0.39, −2.03. HRMS (DART): $[M + H]^+$($C_{42}H_{47}N_8O_4Si_5$), *m*/*z* calcd for: 867.25611, *m*/*z* found: 867.25656.

^{n}(Si$_3$O)$_2$SiPc

Silicon phthalocyanine dichloride (1.00 g, 1.64 mmol) was added into a two-neck round bottom flask equipped with a reflux condenser and three nitrogen-vacuum cycles were performed. The flask was subsequently filled with 80 mL of dry toluene, triethylamine (8 mL, 57.4 mmol) and 1,1,3,3,5,5,5-heptamethyltrisiloxan-1-ol (1.17 g, 4.9 mmol) and the resulting mixture was sparged with N_2 for 10 minutes before heating to reflux overnight. After cooling to rt., the mixture was filtered on a fine frit and the remaining solids were rinsed with DCM until the solvent came out clear. After removing the solvent under vacuum, the product was purified by column chromatography on silica gel (eluent: Hexane 100% to DCM/Hexane = 1/3), affording **^{n}(Si$_3$O)$_2$SiPc** as a blue crystalline solid in 40% yield (666 mg). ^{1}H NMR (600 MHz, $CDCl_3$) δ 9.66–9.62 (m, 8H), 8.37–8.28 (m, 8H), −0.63 (s, 18H), −1.36 (s, 12H), −2.86 (s, 12H). ^{13}C NMR (151 MHz, $CDCl_3$) δ 148.88, 136.29, 130.72, 123.69, 1.21, −0.42, −2.25. HRMS (DART): $[M + H]^+$($C_{46}H_{59}N_8O_6Si_7$), *m*/*z* calcd for: 1015.29369, *m*/*z* found: 1015.29427.

^{iso}(Si$_3$O)$_2$SiPc

Silicon phthalocyanine dichloride (1.00 g, 1.64 mmol) was added into a two-neck round bottom flask equipped with a reflux condenser and three nitrogen-vacuum cycles were performed. The flask was subsequently filled with 80 mL of dry toluene, triethylamine (8 mL, 57.4 mmol) and 1,1,1,3,5,5,5-heptamethyltrisiloxan-3-ol (1.17 g, 4.9 mmol) and the resulting mixture was sparged with N_2 for 10 minutes before heating to reflux overnight. After cooling to rt., the mixture was filtered on a fine frit and the remaining solids were rinsed with DCM until the solvent came out clear. After removing the solvent under vacuum, the product was purified by column chromatography on silica gel (eluent: Hexane 100% to DCM/Hexane = 1/3), affording **^{iso}(Si$_3$O)$_2$SiPc** as a blue crystalline solid in 50% yield (832 mg). ^{1}H NMR match previously reported characterization.[35]

(Si$_4$O)$_2$SiPc

Silicon phthalocyanine dichloride (1.00 g, 1.64 mmol) was added into a two-neck round bottom flask equipped with a reflux condenser and three nitrogen-vacuum cycles were performed. Then the flask was filled up with 50 mL of dry 1,2-dichlorobenzene and tris(trimethylsiloxy)silanol (1025 mg, 3.28 mmol). Subsequently, the mixture was sparged with N_2 for 10 minutes before being heated to reflux overnight, and then cooled to rt. The mixture was poured into 200 mL of cold MeOH to precipitate out the compound. The compound was separated from the mixture using a fine frit and the compound was then redissolved using DCM. After removing the solvent

under vacuum, the crude was purified by column chromatography on silica gel (eluent: Hexane to DCM/Hexane = 1/9), affording **$(Si_4O)_2$SiPc** as a blue crystalline solid in 61% yield (1.16 g). ^{1}H NMR (600 MHz, $CDCl_3$) δ 9.65–9.61 (m, 8H), 8.32–8.28 (m, 8H), −1.18 (s, 54H). ^{13}C NMR (151 MHz, $CDCl_3$) δ 148.99, 136.42, 130.37, 123.59, 0.11. HRMS (DART): $[M + H]^+$ ($C_{50}H_{71}N_8O_8Si_9$), *m*/*z* calcd for: 1163.33128, *m*/*z* found: 1163.33166.

Material characterization

^{1}H and ^{13}C, NMR spectra were recorded on Bruker Avance III HD 600 MHz NMR spectrometer. ^{1}H and ^{13}C NMR chemical shifts were reported in parts per million (ppm) using residual solvent signal as reference. High-resolution mass spectrum was obtained on a JEOL AccuTOF Plus 4G equipped with a Direct Analysis in Real Time (DART) ion source. Analysis was conducted by the Advanced Instrumentation for Molecular Structure Laboratory at the University of Toronto.

Thermogravimetric Analysis was performed using a TA/Waters Discovery 5500, TRIOS v5.5.1 analysis unit. Measurements were conducted under a 25 mL min^{-1} flow of dry nitrogen. Samples were preheated to 70 °C for five minutes to bake out any adsorbed moisture, and then heated at 10 °C min^{-1} to a maximum temperature of 700 °C.

The UV-vis spectra were measured using an Agilent Technologies Cary 6000 UV-vis-NIR spectrophotometer. Absorbance measurements were collected at ambient temperature in solution with DCM as the solvent, at a concentration of $\approx 1.10^{-6}$ mol L^{-1}, within the range 250–800 nm, and on thin films on glass substrates within the range 320–900 nm.

The electrochemical experiments were carried out under argon using a Bioanalytical Systems Inc. (BASi) Epsilon potentiostat with a C3 cell stand and a glass cell and were recorded using BASi Epsilon EC software (V 2.13.77 (c) 2013BASi). For cyclic voltammetry, a three-electrode configuration was employed with a platinum disk (d = 1.6 mm) as the working electrode and platinum wires for the reference and counter electrodes. All potentials were internally referenced to the ferrocene/ferrocenium couple. For the measurements, concentrations of 10^{-3} M of the electroactive species were used in freshly distilled and degassed dichloromethane and 0.1 M tetrabutylammonium hexafluorophosphate.

UPS data were collected at Surface Science Western (Western University, London, Ontario, Canada). The UPS analyses were carried out with a Kratos AXIS Supra X-ray photoelectron spectrometer using a He(I) source (21.22 eV, 30 mA). Analyses were carried out with an analysis area of 110 × 110 microns and a pass energy of 10 eV. A 9 Volt offset is applied during sample analysis (corrected out in the spectra). Samples were electrically well connected to the spectrometer sample stage using copper tape. Energy levels were independently calculated from UPS spectra using gold as a reference.

OTFT device fabrication

BGTC OTFTs were constructed using n-doped Ossila Si substrates with a thermally grown 230 nm thick dielectric layer of SiO_2. The substrates were first cleaned by sonication (VWR ultrasonic cleaner (model no. 97043-964)) in acetone for 5 min. Afterward, the substrates were rinsed with isopropanol and dried under a N_2 stream and plasma treated for 15 min under vacuum. Plasma treatment was performed using a Harrick plasma cleaner (PDC-32G). The plasma-treated substrates were then rinsed sequentially with water and isopropanol, dried under a N_2 stream, submerged in a 1% v/v solution of n-octadecyltrichlorosilane (ODTS) in toluene, and left to react for 1 h at 70 °C. The treated substrates were then sequentially rinsed with toluene and isopropanol, dried under a N_2 stream, annealed under vacuum for 1 h at 70 °C, then subsequently transferred into a glovebox. Following all of the surface treatments, 50 nm of R_2SiPc was deposited onto the substrates *via* physical vapor deposition (PVD) at a rate of 0.2 Å s^{-1} under vacuum ($P < 2 \times 10^{-6}$ Torr). The films were then annealed on a hot plate (T = 80 °C and T = 120 °C) or in an oven (T = 160 °C) for 30 minutes under a nitrogen atmosphere. Afterward, the substrates were placed in a source–drain shadow mask (L = 30 μm, W = 1000 μm) purchased from Ossila. A 50 nm-thick layer of Au was deposited onto the substrates at a rate of 0.5 Å s^{-1} under vacuum ($P < 2 \times 10^{-6}$ Torr). Each substrate was patterned with 20 unique transistors.

OTFT testing

Electrical testing was done at ambient conditions using a custom-built autotester.[39,40] A Keithley 2614B instrument was used to set the gate–source voltage (V_{GS}) and drain–source voltage (V_{DS}) and measure the drain–source current (I_{DS}). All OTFTs were tested for p-type characteristics by fixing V_{GS} at discrete values between 0 V and −50 V or between 0 V and −60 V. During the measurement of transfer characteristics, V_{GS} was applied at a duty cycle of 20% and a frequency of 10 Hz to reduce gate bias stress. Each device's transfer curve was tested four times, measured in the saturation regime, and was modeled using eqn (1).

$$I_{DS} = \frac{\mu C_i W}{2L}(V_{GS} - V_T)^2 \quad (1)$$

where L and W are the channel length and width, respectively. C_i is the capacitance density of the gate dielectric, calculated using eqn (2).

$$C_i = \frac{\varepsilon_0 \varepsilon_r}{t} \quad (2)$$

where t is the dielectric thickness (230 nm), ε_r is the relative dielectric constant of SiO_2 (3.9), and μ_h is the field-effect mobility and is calculated from the slope of the best fit of the $\sqrt{I_{DS}}$ through the most linear region of plotted against V_{GS}. The $\mu_{h,avg}$ represents the calculated mean of n working transistors for each condition, and $\mu_{h,max}$ represents the maximum calculated μ_h for each set of conditions. The threshold voltage (V_T) is calculated as the x-intercept of the same line fitting.

Single-crystal X-ray diffraction

Crystallographic data collection and processing were performed by the X-Ray Core Facility at the University of Ottawa. Crystals were mounted on MiTeGen sample holders using Parabar oil. Data were collected on a Bruker Kappa diffractometer equipped with an ApexII CCD detector and a sealed-tube Mo K source (λ = 0.71073 Å).

PXRD

XRD measurements of the thin films were performed using a Bruker D8 Endeavor diffractometer in reflection mode equipped with a sealed-tube Cu-Kα (λ = 1.5418 Å) source. Measurements were taken directly from thin films deposited on surface-treated substrates with a scan range of $3^\circ < 2\theta < 20^\circ$ and a scan rate of 0.5° min^{-1} with no spin.

2D-XRD

2D XRD measurements of the thin films were performed using a Bruker D8 Discover diffractometer in reflection mode equipped with a sealed-tube Cu-Kα (λ = 1.5418 Å) source. Measurements were taken directly from thin films deposited on surface-treated substrates with a scan range of $3^\circ < 2\theta < 30^\circ$ and a scan rate of approximately 1° min^{-1}.

AFM

AFM images were collected as 10 × 10 μm scans with a Bruker Dimension FastScan using TESPA-V2 probes in PeakForce Tapping ''ScanAsyst'' Mode with 512 samples per line. Image processing was completed using Nanoscope Analysis v.3.0.

Results and discussion

Synthesis and initial characterization

In our previous report, **^{iso}(Si$_3$O)$_2$SiPc** was synthesized in only one step from Cl_2-SiPc using a nucleophilic substitution with a silanol,[35] affording **^{iso}(Si$_3$O)$_2$SiPc** in a moderate yield (36%). The same strategy was successfully employed to synthesize the other analogs described herein, yet these conditions unfortunately led to relatively poor yields such as 13% for **(Si$_2$O)$_2$SiPc**, 18% for **^{n}(Si$_3$O)$_2$SiPc** and only 7% for **(Si$_4$O)$_2$SiPc**. To improve yields, chlorobenzene was substituted with 1,2-dichlorobenzene and the reaction temperature was increased to 180 °C. While this strategy was very beneficial for **(Si$_4$O)$_2$SiPc** with an increased yield of 61%, for the other derivatives only a mixture of inseparable siloxane-SiPcs were obtained. High temperatures appear to favor the disproportionation reaction of the siloxane chains leading to the formation of siloxane chains with undesired chain length and branching. To overcome this challenge, another protocol was designed for **(Si$_2$O)$_2$SiPc**, **^{n}(Si$_3$O)$_2$SiPc** and **^{iso}(Si$_3$O)$_2$SiPc**, in which nucleophilic substitution was carried out in toluene with a large excess of triethylamine. By adding a base, the yields were significantly increased to 54%, 40% and 50%, respectively.

The spectroscopic properties of (Si$_x$O)$_2$SiPcs were investigated in dilute DCM solutions (Fig. 2). All compounds exhibit the same absorption profile, typical of phthalocyanine derivatives, with a Q-band located at 668 nm (see Table 1). This perfect overlap of the UV-Vis traces indicates that the nature of the solubilizing chain does not affect the bandgap energy. The electrochemical behavior of (Si$_x$O)$_2$SiPcs were studied by cyclic voltammetry (CV) in DCM solution and at different scan rates (Fig. 2), all derivatives display a reversible reduction process between −1.43 V *vs.* Fc^+/Fc and −1.22 V *vs.* Fc^+/Fc, as well as a reversible oxidation process between +0.38 V *vs.* Fc^+/Fc and +0.45 V *vs.* Fc^+/Fc (see Table 1). Moreover, these processes remain reversible at every scan rate, displaying their good electrochemical stabilities. All the siloxane chains do not seem to significantly influence either the reduction or oxidation processes except for **(Si$_4$O)$_2$SiPc**, which displays the lowest reduction potential; thus, the presence of sterically hindered siloxane chains seems to impede the reduction process. As the number and the branching of siloxane units in the chain should not lead to any major electronic effect, it was anticipated that the substituents will have very little to no impact on the UV-Vis and CV, as observed.

The UV-Vis absorption profiles of (Si$_x$O)$_2$SiPcs were also investigated in thin films (Fig. 2). All derivatives display clear broadening and red-shifting of their absorption profiles compared to solution studies (see Table 1). Notably, **(Si$_4$O)$_2$SiPc** exhibits the smallest shift (λ_{max}^{film} **(Si$_4$O)$_2$SiPc** = 715 nm) whereas **^{iso}(Si$_3$O)$_2$SiPc** displays the highest one (λ_{max}^{film} **^{iso}(Si$_3$O)$_2$SiPc** = 747 nm). Interestingly, both derivates containing linear siloxane chains display very similar absorption maxima: λ_{max}^{film} **(Si$_2$O)$_2$SiPc** = 736 nm and λ_{max}^{film} **^{iso}(Si$_3$O)$_2$SiPc** = 731 nm. The complete similarity of all the UV-Vis traces in solution in contrast to the relatively significant changes observed in the thin films indicate that (Si$_x$O)$_2$SiPcs undergo aggregation in the solid state. Moreover, the nature of the chain seems to impact the aggregation in a unique way for every derivative as all the UV-Vis traces are different in the solid state.

Table 1 Optical, electrochemical, and UPS characterization of (Si$_x$O)$_2$SiPcs

Compound	λ_{MAX} DCM/film (nm)	E_{gap}[a] (eV)	E_{onset}^{ox} (V *vs.* Fc^+/Fc)	E_{onset}^{red} (V *vs.* Fc^+/Fc)	Φ[b] (eV)	Δe[b] (eV)	HOMO/LUMO$_{UPS}$[b] (eV)
(Si$_2$O)$_2$SiPc	668/736	1.6	+0.40	−1.25	3.2	1.8	−5.0/−3.4
^{n}(Si$_3$O)$_2$SiPc	668/731	1.7	+0.45	−1.22	3.2	1.7	−4.9/−3.2
^{iso}(Si$_3$O)$_2$SiPc[c]	668/747	1.6	+0.43	−1.27	3.2	1.7	−4.9/−3.3
(Si$_4$O)$_2$SiPc	668/715	1.6	+0.38	−1.43	3.2	1.7	−4.9/−3.3

[a] The optical band gap was characterized using the onset of the absorption in thin film. [b] Energy levels and work function were estimated from UPS spectra with a +9 V bias and 21.22 eV emission source and calibrated using an Au reference. We estimated the ionization energy (IE) to be equal to the HOMO energy level, and LUMO = HOMO + $E_{G,film}$. [c] All the data for **^{iso}(Si$_3$O)$_2$SiPc** were taken from Ledos *et al.*[35]

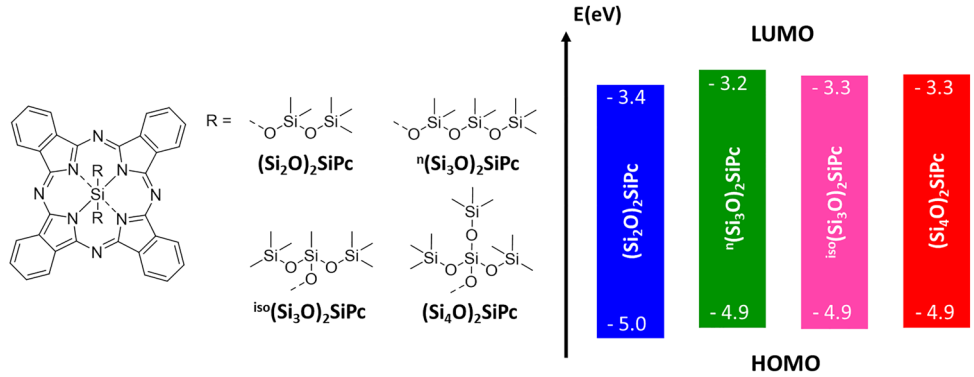

Fig. 1 Chemical structure (left) and frontier orbitals energy diagram (right) of $(Si_xO)_2$SiPcs, obtained by UPS and thin film UV-Vis absorption.

The highest occupied molecular orbital (HOMO) and lowest unoccupied molecular orbital (LUMO) energy levels were estimated using UPS and thin film absorption spectra (see Table 1): HOMO energy level values were estimated from the ionization potential (IP) which was obtained from the work function (Φ) and offset (Δe) determined by UPS, while the LUMO energy levels were estimated from the HOMO levels and solid state E_G determined by UV-Vis. By these means, the HOMO levels of each derivative can be estimated to be between −4.9 and −5.0 eV while the LUMO energy levels are estimated between −3.2 and −3.4 eV (Fig. 1 and Fig. S1). These values are once again very similar and it was anticipated that all the derivatives should behave as p-type semiconductors as previously reported for **^{iso}(Si$_3$O)$_2$SiPc**.[35]

Slow evaporation of concentrated solutions of **(Si$_2$O)$_2$SiPc**, **^{n}(Si$_3$O)$_2$SiPc**, and **(Si$_4$O)$_2$SiPc** in DCM produced large crystals suitable for single crystal X-ray diffraction (SC-XRD) analysis. In addition to the crystalline structures of **^{iso}(Si$_3$O)$_2$SiPc** already described in the literature,[35,41] the crystal structure of every $(Si_xO)_2$SiPc described herein has been resolved. Two different polymorphs of **^{iso}(Si$_3$O)$_2$SiPc** can be obtained, which crystallize in the $P2_1/c$ and the $P2_1/n$ space groups. In both structures, the Pc rings display π-stacking interactions along two crystallographic axes, and arrange themselves in a typical brick-like array of molecules, making them compatible with 2D hopping transport. A single polymorph of **(Si$_4$O)$_2$SiPc** has been isolated, crystallizing in the $P\bar{1}$ space group. In this structure the Pc rings are also π-stacking along two crystallographic axes (both the *a*-axis and the *b*-axis), and arrange in a brick-like array of molecules as highlighted in Fig. S6. The Pc rings are packed very closely within the crystal, the smallest short π–π contact along the *a*-axis is equal to 3.30 Å and equal to 3.32 Å along the *b*-axis. For **(Si$_2$O)$_2$SiPc**, a polymorph has been isolated from solution, crystallizing in the $P\bar{1}$ space group. In this material, the Pc rings in the structure exhibit π-stacking only along one crystallographic axis (the *a*-axis, see Fig. S5) with the smallest short π–π contact being equal to 3.52 Å. Lastly, two polymorphs of **^{n}(Si$_3$O)$_2$SiPc** have been isolated with both crystallizing in the $P2_1/c$ space group of the monoclinic system (Fig. S3 and S4). Interestingly, the two distinct polymorphs were obtained within the same starting solution (also known as concomitant polymorphs), which highlights the high number of energy-equivalent conformers made possible by a longer linear siloxane chain. Both structures display Pc rings exhibiting π-stacking along the *c*-axis only yet slight discrepancies in their packing are noted. For the first polymorph (polymorph 1), the smallest π–π contact along the *c*-axis is equal to 3.45 Å, while this value is equal to 3.49 Å for polymorph 2. To summarize, the presence of linear siloxane substituents allows the formation of polymorphs displaying π-stacking along only one crystallographic axis as well as large

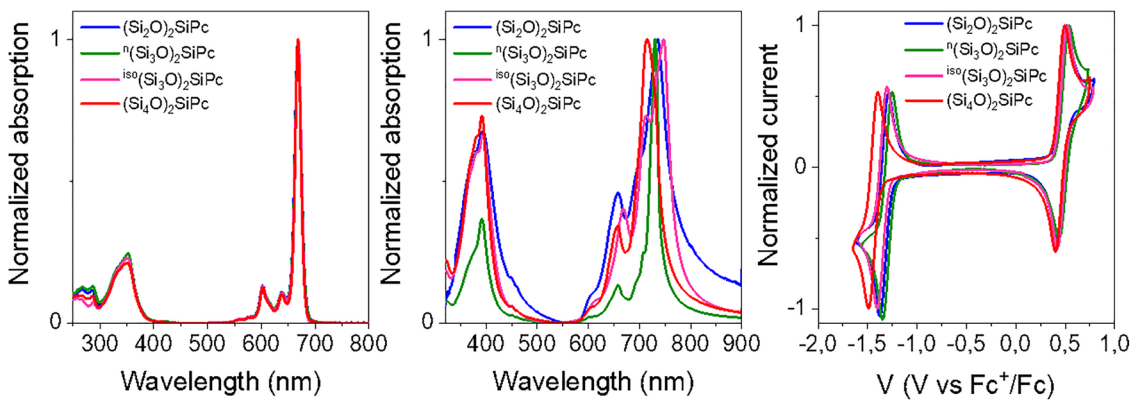

Fig. 2 UV-Vis absorption in DCM solution (left), in thin film (middle) and cyclic voltammetry (right) of $(Si_xO)_2$SiPcs. All the data for **^{iso}(Si$_3$O)$_2$SiPc** were taken from Ledos *et al.*[35]

π-stacking distances. Conversely, the presence of branched siloxane substituents allows the formation of polymorphs displaying brick-like arrays of Pc rings, compatible with 2D hopping transport, and smaller π-stacking distances. Thus, branched siloxane derivatives seem to be better candidates for OTFT applications.

OTFT fabrication and characterization

OTFTs containing $(Si_xO)_2$SiPcs as the semiconductors were fabricated by PVD, onto ODTS-treated SiO_2 dielectric substrates, using a bottom gate top contact (BGTC) configuration. Twenty transistors were fabricated on each substrate using PVD to deposit patterned gold electrodes, with channel lengths of 30 μm and channel widths of 1000 μm. Although the high solubility of $(Si_xO)_2$SiPcs in organic solvents enables the fabrication of OTFTs using a solution process, we decided to use the optimized vapor deposition method developed previously for **^{iso}(Si$_3$O)$_2$SiPc** to ensure an accurate comparison with the newly synthesized $(Si_xO)_2$SiPcs.[35] Due to the anticipated p-type character of all $(Si_xO)_2$SiPcs, gold electrodes were used for all devices and all the electrical measurements were performed in air (see Fig. 3 and Table S2). Neat films of $(Si_xO)_2$SiPcs led to devices with $\mu_{h,avg} = 1.3 \times 10^{-3}$ cm^2 V^{-1} s^{-1} and $V_T = -41.8$ V for **^{n}(Si$_3$O)$_2$SiPc** compared to $\mu_{h,avg} = 0.32$ cm^2 V^{-1} s^{-1} and $V_T = -18.7$ V for **^{iso}(Si$_3$O)$_2$SiPc**. **(Si$_2$O)$_2$SiPc** displays moderate performance ($\mu_{h,avg} = 5.8 \times 10^{-2}$ cm^2 V^{-1} s^{-1} and $V_T = -35.4$ V) and **(Si$_4$O)$_2$SiPc** displays high mobility but high V_T ($\mu_{h,avg} = 0.14$ cm^2 V^{-1} s^{-1} and $V_T = -28.6$ V). Interestingly, the chain length seems not to be the main factor influencing the performances as **^{n}(Si$_3$O)$_2$SiPc** and **^{iso}(Si$_3$O)$_2$SiPc** gave rise to both the best and worst performing films. On the other hand, both branched derivatives, **^{iso}(Si$_3$O)$_2$SiPc** and **(Si$_4$O)$_2$SiPc** display the best performances. The neat films with higher $\mu_{h,avg}$ were also characterized with a lower V_T.

The effect of thermal annealing on electrical performance was also investigated. Films of $(Si_xO)_2$SiPcs were annealed in a glove box at 80, 120 or 160 °C for 30 minutes. Each $(Si_xO)_2$SiPc displayed unique behavior. In the case of **(Si$_2$O)$_2$SiPc** and **^{n}(Si$_3$O)$_2$SiPc**, the best $\mu_{h,avg}$ were obtained at 80 °C ($\mu_{h,avg} = 7.2 \times 10^{-2}$ cm^2 V^{-1} s^{-1} and $\mu_{h,avg} = 3.4 \times 10^{-3}$ cm^2 V^{-1} s^{-1}, respectively), a further increase in the annealing temperature led to an increased V_T and a decreased $\mu_{h,avg}$ for **(Si$_2$O)$_2$SiPc**, while for **^{n}(Si$_3$O)$_2$SiPc** both V_T and $\mu_{h,avg}$ decreased. Concerning the two branched derivatives, **^{iso}(Si$_3$O)$_2$SiPc** and **(Si$_4$O)$_2$SiPc**, the best $\mu_{h,avg}$ were reached after annealing at 160 °C ($\mu_{h,avg} = 1.01$ cm^2 V^{-1} s^{-1} and $\mu_{h,avg} = 0.21$ cm^2 V^{-1} s^{-1}, respectively). However, while for **^{iso}(Si$_3$O)$_2$SiPc** the $\mu_{h,avg}$ of annealed films are all superior to the neat film, this is not the case for **(Si$_4$O)$_2$SiPc** in which the $\mu_{h,avg}$ first decreases to a minimum at 80 °C ($\mu_{h,avg} = 3.6 \times 10^{-2}$ cm^2 V^{-1} s^{-1}) before increasing. The impact of the annealing temperature on the V_T is rather minimal for those two compounds: the V_T slightly decreases from −18.7 V at r.t to −15.9 V at 160 °C for **^{iso}(Si$_3$O)$_2$SiPc** while V_T remains similar ($V_T \approx -30$ V) at every temperature in the case of **(Si$_4$O)$_2$SiPc**. Overall, these results demonstrate that choice of axial substituents heavily influences device performance and the effect of annealing. Mainly, branched siloxane derivatives led to the best performing devices, with mobility up to three orders of magnitude above the devices made with linear siloxane derivatives.

Thin film characterization

Powder X-ray diffraction (PXRD) was used to characterize the crystallinity of $(Si_xO)_2$SiPcs thin films as a function of annealing temperature (Fig. 4). The PXRD trace of **(Si$_2$O)$_2$SiPc** thin films display the weakest intensity of the series, with the film at RT exhibiting only one peak at $2\theta = 8.6°$. After thermal annealing, the film displays important changes: upon treatment at 80 °C, the intensity of the peak at $2\theta = 8.6°$ increases and the second order harmonic peak at $2\theta = 17.2°$ appears. Concomitantly, a new peak at a lower $2\theta = 7.3°$ value appears indicating the formation of a new polymorph. After the treatment at 120 °C, the peak at $2\theta = 8.6°$ almost disappears while the one at $2\theta = 17.2°$ completely disappears as the intensity of the new polymorph peak increases. After the annealing at 160 °C, only

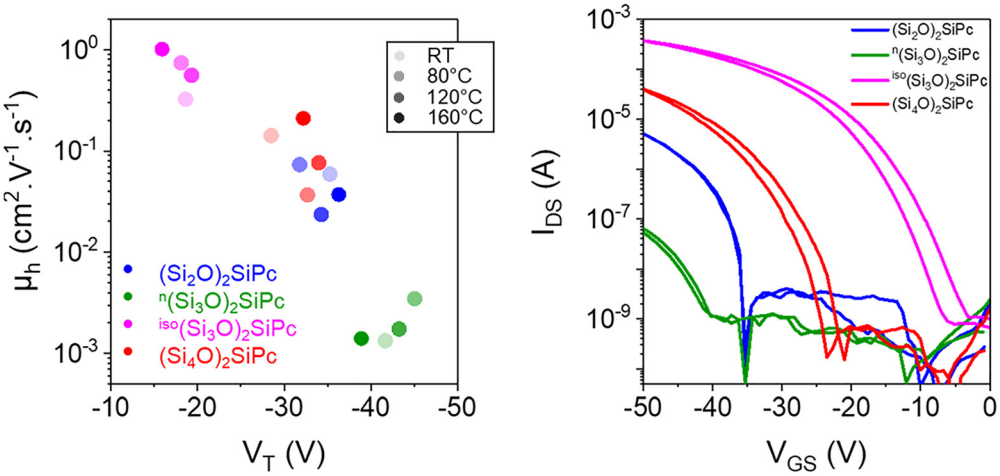

Fig. 3 Average electrical characteristics of $(Si_xO)_2$SiPc OTFTs prepared using different annealing temperatures (left). Characteristic transfer curves of $(Si_xO)_2$SiPcs OTFTs ($V_{DS} = -50$ V) thermally annealed at 160 °C for 30 minutes (right). All the data for **^{iso}(Si$_3$O)$_2$SiPc** were taken from Ledos *et al.*[35]

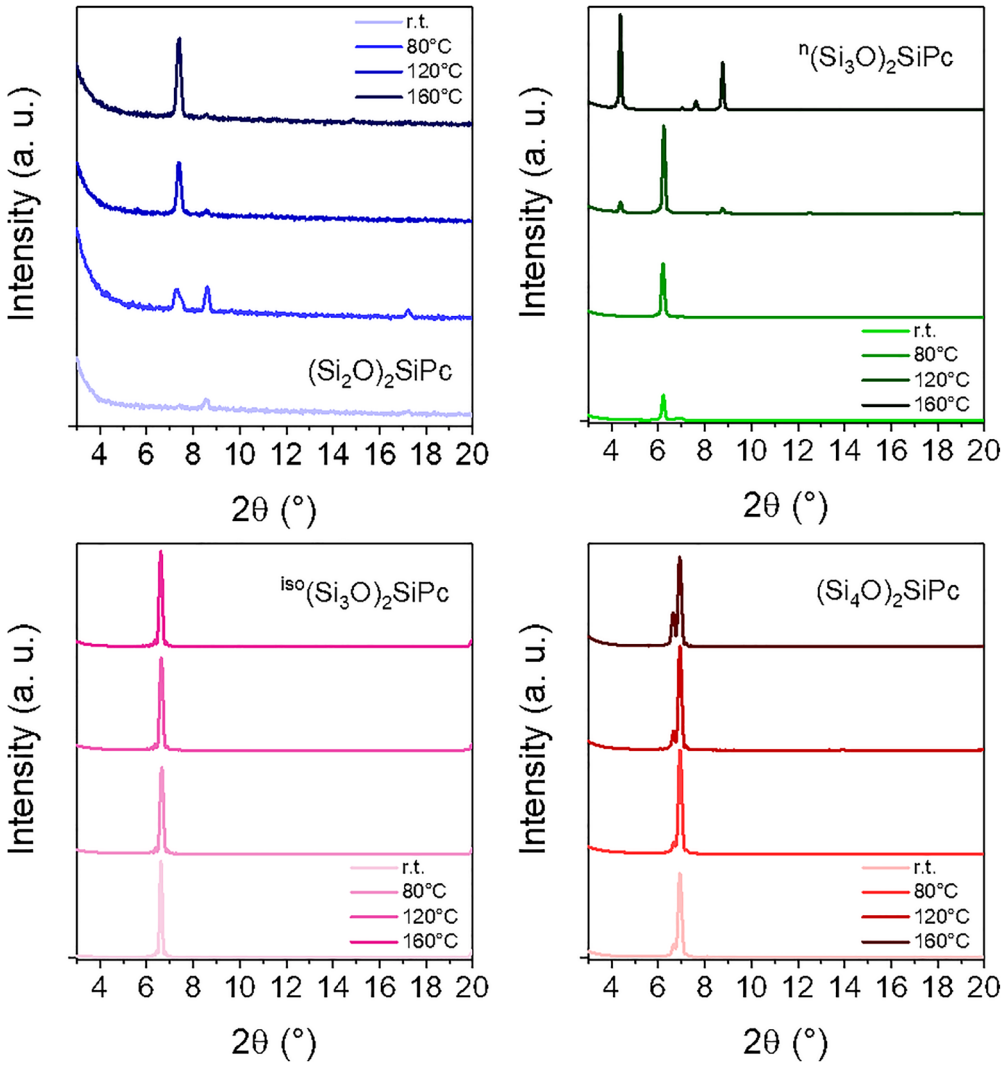

Fig. 4 PXRD trace of $(Si_xO)_2$SiPcs thin films on ODTS-treated SiO_2 surfaces annealed at various temperatures.

the peak at $2\theta = 7.3^\circ$ remains at a higher intensity indicating a complete transition from one polymorph, once the film was deposited, to a second one, formed gradually at higher temperatures. It is worth mentioning that neither of the two polymorphs matches the SC-XRD predicted PXRD trace calculated from the single crystals isolated from solution. The PXRD trace of thin films of **^{n}(Si$_3$O)$_2$SiPc** are highly diffracting and display very intense peaks; at RT the film shows one peak of high intensity at $2\theta = 6.2^\circ$, two peaks of moderate intensity at $2\theta = 6.8^\circ$ and 7.0° and several peaks of very weak intensities at $2\theta = 7.6^\circ$, 12.5°, 14.2° and 18.8° (higher harmonic order peaks) indicating the presence of several polymorphs. Thermal annealing strongly impacts films of **^{n}(Si$_3$O)$_2$SiPc**, after the treatment at 80 °C the peaks at $2\theta = 6.8^\circ$ and 7.6° disappear and intensity of the most intense peak doubled, indicating a rearrangement of the film into one or two polymorphs and an increased crystallinity of the film. After the treatment at 120 °C, the intensity of the peak at $2\theta = 6.2^\circ$ continues to increase and a new set of peaks appear at $2\theta = 4.4^\circ$, 7.6° and 8.8° indicating the formation of a new polymorph and the reappearance of the polymorph present at RT. At 160 °C, the peaks at $2\theta = 6.2^\circ$, 12.5° and 18.8° fully disappear, and the peaks at $2\theta = 4.4^\circ$ and 8.8° become predominant. Thus, the polymorph formed at 120 °C becomes the most abundant one at 160 °C coexisting with at least one other polymorph. Overall, **^{n}(Si$_3$O)$_2$SiPc** thin films undergo complex changes in crystallinity when thermally annealed with the appearance and disappearance of numerous different polymorphs (see the phase diagram summarizing the main change in Fig. S8). Moreover, none of the previously described peaks match the SC-XRD predicted PXRD traces calculated from single crystals isolated from solution. Thin films of **^{iso}(Si$_3$O)$_2$SiPc** deposited on ODTS-treated SiO_2 are highly diffracting as previously reported.[35] The neat film displays one single peak at $2\theta = 6.6^\circ$ and the onset of a second peak can be seen at $2\theta = 20.0^\circ$. Using the single crystal data from Yu *et al.* these peaks can be attributed to the (020) and (060) planes, respectively, of their described polymorph.[41] Interestingly, the PXRD traces of **^{iso}(Si$_3$O)$_2$SiPc** are completely unaffected by thermal

annealing up to 160 °C, as all the traces remain unchanged and keep the same intensity.

Thin films of **$(Si_4O)_2$SiPc** are also highly diffracting, the neat film displays one low-intensity peak at $2\theta = 6.7°$ followed by one very intense peak at $2\theta = 6.9°$. Using the SC-XRD collected on the polymorph isolated from solution we attributed the latter peak to the (001) plane. The presence of only one second peak having a very similar *d*-spacing might indicate to us that the film is composed of two polymorphs having very close cell parameters. Moreover, thermal annealing at higher temperatures led to a slight increase in the intensity of the low-angle peak and a slight decrease in the intensity of the higher-angle peak, making **$(Si_4O)_2$SiPc** thin film crystallinity also resilient toward thermal annealing. Overall, **$(Si_2O)_2$SiPc** and **$^{n}(Si_3O)_2$SiPc** thin films experienced significant changes in crystallinity when thermally annealed, especially for **$^{n}(Si_3O)_2$SiPc** (see Fig. S8). However, both **$^{iso}(Si_3O)_2$SiPc** and **$(Si_4O)_2$SiPc** exhibit negligible changes in crystallinity upon thermal annealing. Therefore, the branched siloxane chains confer more robustness toward heat compared to linear siloxane chains. We surmise the higher flexibility and the high number of energy-equivalent conformers available from linear chains give the possibility to form a wider range of polymorphs. This is especially the case when the chains are longer and is well-illustrated by **$^{n}(Si_3O)_2$SiPc**: concomitant polymorphs were obtained from solution, and thin films experienced the most significant changes once annealed. The presence of multiple polymorphs in **$^{n}(Si_3O)_2$SiPc** thin films may be one of the reasons why OTFTs made from this derivative did not perform as well, as efficient charge carrier transport is more likely to occur in a uniform crystalline motif. Overall, the branched siloxane chain based SiPcs tend to generate fewer polymorphs compared to linear siloxane chains which suggests the films are more stable to processing conditions and could support their improved OTFT performances.

The crystalline texture of $(Si_xO)_2$SiPcs thin films was investigated with respect to the annealing temperature using 2D X-ray diffraction (2D-XRD) (Fig. 5). By using a 2D X-ray detector, we can estimate the uniformity of the crystalline texture of the different films (*i.e.*, how uniform is the orientation of the crystallites within the film). Moving from 1D to 2D-XRD,

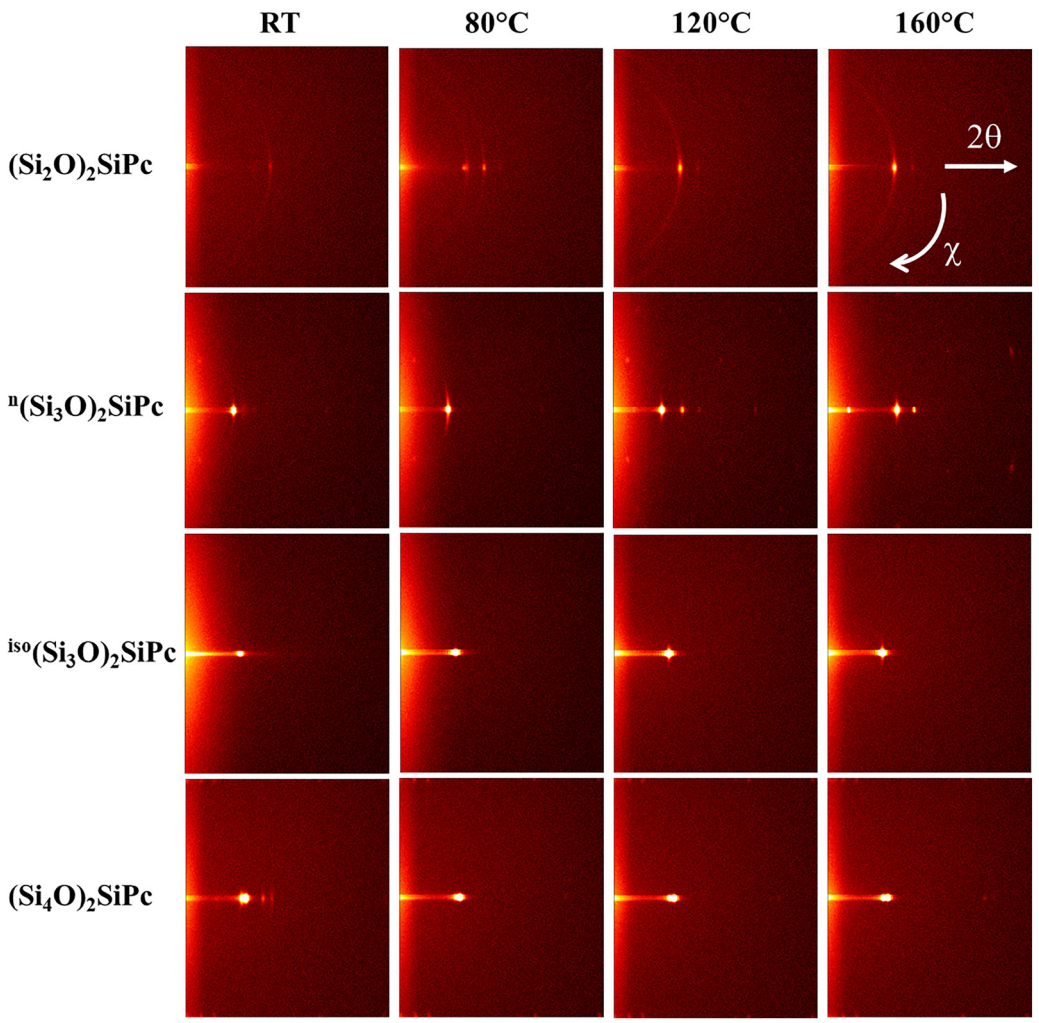

Fig. 5 2D-XRD maps of $(Si_xO)_2$SiPcs thin films on ODTS-treated SiO_2 surfaces annealed at various temperatures. All the maps range from $2\theta = 3°$ to 15° on the *Y*-axis, from the left to the right. Full maps taken from $2\theta = 3°$ to 30° with peak labels are available in the SI (Fig. S9–S24).

the diffusion of reflection spots along the χ angle provides information on the crystalline texture of the films. The presence of single spots, arcs or rings, respectively, indicates highly ordered, poorly ordered or disordered crystallite orientation within the film.[42] All **$(Si_2O)_2$SiPc** films display ring-like reflections with weak intensity, indicating the absence of preferential crystallite orientation. **$^{n}(Si_3O)_2$SiPc** films display maps featuring arcs of various radii along the χ angle. Neat films and films annealed at 80 °C display larger radii, indicating preferential crystallite orientation. In contrast, films annealed at 120 °C and 160 °C only display dot-like reflection features, indicating that higher annealing temperatures promote the organization of the crystallites within the film. In contrast, both **$^{iso}(Si_3O)_2$SiPc** and **$(Si_4O)_2$SiPc** films display only single spots and do not undergo any significant change with thermal annealing. Thus, these two compounds, which possess branched siloxane axial substituents, display a very uniform crystalline texture that is unaffected by thermal annealing.

Analysis of the X-ray diffraction of $(Si_xO)_2$SiPcs thin films using 1D and 2D detectors revealed distinct behaviors between linear and branched siloxane-substituted SiPc. The branched derivatives displayed very intense diffraction patterns, a small number of coexisting polymorphs, an extremely uniform crystalline texture, and high resilience toward thermal annealing. Conversely, the linear derivatives exhibit weak to intense diffraction patterns, a large number of coexisting polymorphs, lower uniformity of crystalline texture, and significant crystalline reorganization upon thermal annealing. Ultimately, we believe that the superior crystalline characteristics of the branched derivatives are responsible for their superior electrical performance.

Finally, we performed an investigation of the morphology of $(Si_xO)_2$SiPcs thin films using atomic force microscopy (AFM) (Fig. 6). Interestingly, all of the films display unique morphologies. **$(Si_2O)_2$SiPc** thin films exhibit a surface composed of thin, superimposed layers. Additionally, the films undergo some degree of reorganization from the pristine film to the one annealed at 160 °C, with an overall increase in roughness and the appearance of more pronounced grain boundaries. Thin films of **$^{n}(Si_3O)_2$SiPc** have very uneven surfaces and large, interconnected crystalline features. Upon annealing, the films undergo considerable reorganization; the crystallites gradually merge to form a thicker crystalline layer and large geometrically shaped holes within the film. In particular, thin films of **$^{n}(Si_3O)_2$SiPc** exhibit very large pinholes that likely inhibit charge transport. Films of **$^{iso}(Si_3O)_2$SiPc** exhibit a uniform surface composed of small crystalline flakes stacked parallel to the substrate. Once annealed, the crystallites gradually fuse together. Large cracks appear in the film at 120 °C, and their widths are significantly reduced at 160 °C. Lastly, **$(Si_4O)_2$SiPc** films also have very smooth, uniform surfaces composed of small, stacked, square crystallites parallel to the substrate.

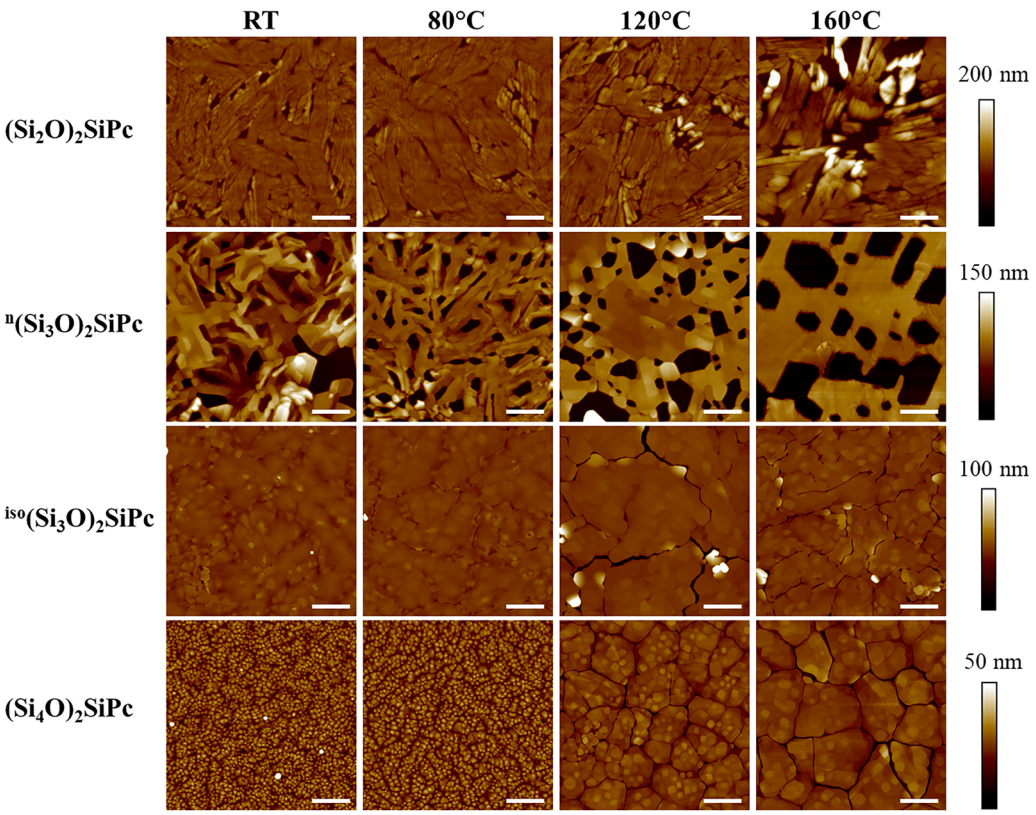

Fig. 6 AFM images of (10 μm × 10 μm, scale bar 2 μm) $(Si_xO)_2$SiPcs films deposited on ODTS-treated SiO_2 with various post-deposition thermal annealing temperatures.

Upon annealing, the crystallites gradually fuse together, forming large crystalline domains surrounded by cracks at 160 °C. Finally, there is good agreement between the observations of 2D-XRD and AFM for both branched derivatives and **^{n}(Si$_3$O)$_2$SiPc** films annealed at 120 and 160 °C. Indeed, they all display highly uniform crystalline textures by 2D-XRD, and AFM imaging shows surfaces composed of crystallites with the same orientation. Analysis of the thin film morphology of (Si$_x$O)$_2$SiPcs demonstrates that branched siloxane derivatives lead to favorable thin film morphology for charge transport applications over their linear counterparts. Branched derivatives form the most uniform and smooth surfaces, whereas linear derivatives produce the roughest, least uniform films.

^{n}(Si$_3$O)$_2$SiPc displays the lowest OTFT performance of the series due to a combination of poor film morphology (rough surface, presence of large pinholes), presence of multiple crystalline phases and a significant crystalline phase transition upon thermal annealing. We attribute this effect of the long linear siloxane chain to its high flexibility and number of conformers that allow such a high degree of mixed crystalline phases and reorganization. **(Si$_2$O)$_2$SiPc** possesses chains having less flexibility, and thus, the number of crystalline phases is reduced and reorganization upon thermal annealing is less apparent. Nevertheless, the presence of a smaller siloxane chain seems to lead to less crystalline films and poorly uniform crystalline texture. As a result, the $\mu_{h,avg}$ of **(Si$_2$O)$_2$SiPc**-based OTFTs is moderate ($\mu_{h,avg} = 7.2 \times 10^{-2}$ cm^2 V^{-1} s^{-1}) and reaches a maximum with thermal annealing at 80 °C, the temperature at which the smoothest film surface is obtained. Finally, both derivatives having branched siloxane substituents, **^{iso}(Si$_3$O)$_2$SiPc** and **(Si$_4$O)$_2$SiPc**, display the highest $\mu_{h,avg}$ of the series; exhibiting a large number of favorable characteristics for efficient charge carrier transport: tight π-stacking, compatible with 2D hopping transport, very high crystallinity, and exceptionally uniform crystalline texture as well as smooth and uniform film morphology. **^{iso}(Si$_3$O)$_2$SiPc** outperforms **(Si$_4$O)$_2$SiPc** by an order of magnitude in $\mu_{h,avg}$ while exhibiting a lower V_T. This can be attributed to the mixed crystalline phases in **(Si$_4$O)$_2$SiPc** thin films, which introduce additional energetic barriers for charge carriers, and to the bulkier siloxane units, which increase the spacing between stacked Pc rings and thereby hinder charge injection from the electrode to the channel.

Conclusion

In this study, a series of four siloxane-SiPc derivatives featuring systematically varied siloxane chain length and branching were synthesized and integrated into OTFTs to evaluate their semiconducting properties. To the best of our knowledge, this represents the first synthesis of **^{n}(Si$_3$O)$_2$SiPc** and the first use of **(Si$_2$O)$_2$SiPc**, **^{n}(Si$_3$O)$_2$SiPc**, and **(Si$_4$O)$_2$SiPc** in OTFT devices. Additionally, careful characterization of the thin film properties was performed using AFM, 1D and 2D XRD as well as UPS. For our series of siloxane-containing OSCs, we established design guidelines: chains must be sufficiently long to promote crystallization and uniform films, while branching helps limit crystalline phase diversity and enables tighter π-stacking. However, the chains should remain as short as possible to minimize spacing between stacked OSC planes separated by insulating siloxane segments. The sweet spot, in this case, was obtained with **^{iso}(Si$_3$O)$_2$SiPc** with its two 1,1,1,3,5,5,5-heptamethyltrisiloxan-3-ol axial substituents. This compound achieves an average mobility above 1 cm^2 V^{-1} s^{-1}, which is almost 3 orders of magnitude higher than **^{n}(Si$_3$O)$_2$SiPc**, its counterpart bearing linear chains. We believe this work underlines the importance of the choice of the side chain when designing a new OSC, brings new comprehensive tools to understand, retrospectively, the efficiency of OSCs bearing 1,1,1,3,5,5,5-heptamethyltrisiloxan-3-ol substituents and provides to the community clear design rules to build new highly efficient OSCs containing siloxane solubilizing chains.

Conflicts of interest

The authors declare no conflicts of interest.

Data availability

All data necessary to support the conclusions of this study are provided in the manuscript and the supplementary information (SI). Supplementary information: UPS spectra, thermogravimetric analysis, predicted powder X-ray diffractogram, ^{1}H and ^{13}C NMR of (Si$_x$O)$_2$SiPcs, HRMS of (Si$_x$O)$_2$SiPcs, full 2D-XRD maps, crystallographic table, table of the average electrical characteristics of (Si$_x$O)$_2$SiPcs OTFTs and every output and transfer curves supporting the electrical characterization results. See DOI: https://doi.org/10.1039/d5qm00722d.

Additional information is available from the corresponding author upon reasonable request.

CCDC 2487841, 2487842, 2487844 and 2487846 contain the supplementary crystallographic data for this paper.[43a–d]

Acknowledgements

We thank Natural Sciences and Engineering Research Council of Canada (NSERC) Discovery program (RGPIN-2025-03936 to B. H. L and RGPIN-2021-04146 to J. L. B.) for supporting this project and NSERC CGS to H. R. L. We thank the Ontario Research Fund (Large Infrastructure Fund) and Canadian Foundation for Innovation, CFI# 40178 (HIIT) and CFI# 43247 (SSMART), for support in acquisition and maintenance of the infrastructure needed for this project. The authors would like to thank Dr Jeffrey Ovens of the University of Ottawa X-ray core facility for acquiring single crystal data and Patrick Pageau of the University of Ottawa Chemical Engineering Machine Shop for designing and machining the substrate mount.

References

1 J. Mei, D. H. Kim, A. L. Ayzner, M. F. Toney and Z. Bao, Siloxane-Terminated Solubilizing Side Chains: Bringing Conjugated Polymer Backbones Closer and Boosting Hole Mobilities in Thin-Film Transistors, *J. Am. Chem. Soc.*, 2011, **133**(50), 20130–20133, DOI: 10.1021/ja209328m.

2 Q. Wang, X. Zhang, W. Zou, H. Xu, Y. Kan, Y. Sun and K. Gao, Silane or Siloxane-Side-Chain Engineering of Photovoltaic Materials for Organic Solar Cells, *Chin. J. Chem.*, 2023, **41**(24), 3703–3713, DOI: 10.1002/cjoc.202300397.

3 B. W. L. Van Den Bersselaar, E. H. W. Cattenstart, K. E. Elangovan, C. Yen-Chi, B. F. M. De Waal, J. Van Der Tol, Y. Diao, E. W. Meijer and G. Vantomme, Trade-off between Processability and Device Performance in Donor–Acceptor Semiconductors Revealed Using Discrete Siloxane Side Chains, *J. Mater. Chem. C*, 2024, **12**(18), 6637–6644, DOI: 10.1039/D4TC00875H.

4 Y. Yuan, F. Zhao, Y. Ding, G. Zhang, X. Wang and L. Qiu, Asymmetric Hybrid Siloxane Side Chains for Enhanced Mobility and Mechanical Properties of Diketopyrrolopyrrole-Based Polymers, *Macromol. Rapid Commun.*, 2022, **43**(3), 2100636, DOI: 10.1002/marc.202100636.

5 S. Liu, Z. You, T. Wu, Y. Feng, J. Cao, L. Hou and Z. Yu, Toward Eco-Friendly Solvent-Processable DPP-Based Conjugated Polymers with Siloxane Branched Side Chains: Synthesis, Properties, and Ambipolar Field-Effect Transistor Characteristics, *ACS Appl. Electron. Mater.*, 2025, **7**(4), 1694–1707, DOI: 10.1021/acsaelm.4c02364.

6 Y. Ding, F. Zhao, S. Kim, X. Wang, H. Lu, G. Zhang, K. Cho and L. Qiu, Azaisoindigo-Based Polymers with a Linear Hybrid Siloxane-Based Side Chain for High-Performance Semiconductors Processable with Nonchlorinated Solvents, *ACS Appl. Mater. Interfaces*, 2020, **12**(37), 41832–41841, DOI: 10.1021/acsami.0c11436.

7 Z. Tang, X. Xu, R. Li, L. Yu, L. Meng, Y. Wang, Y. Li and Q. Peng, Asymmetric Siloxane Functional Side Chains Enable High-Performance Donor Copolymers for Photovoltaic Applications, *ACS Appl. Mater. Interfaces*, 2020, **12**(15), 17760–17768, DOI: 10.1021/acsami.9b20204.

8 R. Qiu, Z. Wu, S. Li, H. Jiang, Q. Wang, Y. Chen, X. Liu, L. Zhang and J. Chen, Replacing Alkyl Side Chain of Non-Fullerene Acceptor with Siloxane-Terminated Side Chain Enables Lower Surface Energy towards Optimizing Bulk-Heterojunction Morphology and High Photovoltaic Performance, *Sci. China Chem.*, 2021, **64**(7), 1208–1218, DOI: 10.1007/s11426-021-9975-9.

9 Z. Yin, X. Guo, Y. Wang, L. Zhu, Y. Chen, Q. Fan, J. Wang, W. Su, F. Liu, M. Zhang and Y. Li, Siloxane-Functional Small Molecule Acceptor for High-Performance Organic Solar Cells with 16.6% Efficiency, *Chem. Eng. J.*, 2022, **442**, 136018, DOI: 10.1016/j.cej.2022.136018.

10 Q. Wang, Z. Hu, Z. Wu, Y. Lin, L. Zhang, L. Liu, Y. Ma, Y. Cao and J. Chen, Introduction of Siloxane-Terminated Side Chains into Semiconducting Polymers To Tune Phase Separation with Nonfullerene Acceptor for Polymer Solar Cells, *ACS Appl. Mater. Interfaces*, 2020, **12**(4), 4659–4672, DOI: 10.1021/acsami.9b18963.

11 Y. Li, S. Song, S. Y. Park, J. Y. Kim and H. Y. Woo, Semi-Crystalline Photovoltaic Polymers with Siloxane-Terminated Hybrid Side-Chains, *Sci. China Chem.*, 2017, **60**(4), 528–536, DOI: 10.1007/s11426-016-0520-6.

12 D. Yuan, F. Pan, L. Zhang, H. Jiang, M. Chen, W. Tang, G. Qin, Y. Cao and J. Chen, Improved Average Figure-of-Merit of High-Efficiency Nonfullerene Solar Cells via Minor Combinatory Side Chain Approach, *Solar RRL*, 2020, **4**(6), 2000062, DOI: 10.1002/solr.202000062.

13 Q. Wang, M. Li, Z. Peng, N. Kirby, Y. Deng, L. Ye and Y. Geng, Calculation Aided Miscibility Manipulation Enables Highly Efficient Polythiophene: Nonfullerene Photovoltaic Cells, *Sci. China Chem.*, 2021, **64**(3), 478–487, DOI: 10.1007/s11426-020-9890-6.

14 J. Mei, H.-C. Wu, Y. Diao, A. Appleton, H. Wang, Y. Zhou, W.-Y. Lee, T. Kurosawa, W.-C. Chen and Z. Bao, Effect of Spacer Length of Siloxane-Terminated Side Chains on Charge Transport in Isoindigo-Based Polymer Semiconductor Thin Films, *Adv. Funct. Mater.*, 2015, **25**(23), 3455–3462, DOI: 10.1002/adfm.201500684.

15 N. Kamatham, O. A. Ibraikulov, P. Durand, J. Wang, O. Boyron, B. Heinrich, T. Heiser, P. Lévêque, N. Leclerc and S. Méry, On the Impact of Linear Siloxanated Side Chains on the Molecular Self-Assembling and Charge Transport Properties of Conjugated Polymers, *Adv. Funct. Mater.*, 2021, **31**(6), 2007734, DOI: 10.1002/adfm.202007734.

16 F. Zhao, Y. Yuan, Y. Ding, Y. Wang, X. Wang, G. Zhang, X. Gu and L. Qiu, Taming Charge Transport and Mechanical Properties of Conjugated Polymers with Linear Siloxane Side Chains, *Macromolecules*, 2021, **54**(12), 5440–5450, DOI: 10.1021/acs.macromol.1c00441.

17 X. Chen, L. Zhang, M. Chen, D. Ma, J. Wang and J. Chen, Diverse Siloxane-Terminated Side Chain Ameliorated Simple Polymer Donors towards Efficient and Stable Air-Processed Organic Solar Cells, *Chem. Eng. J.*, 2025, **504**, 158404, DOI: 10.1016/j.cej.2024.158404.

18 C. M. Udamulle Gedara, Z. Ma, M. M. Talukder, R. Gunawardhana, M. C. Biewer and M. C. Stefan, Siloxane Side-Chain-Modified Diketopyrrolopyrrole and Thienopyrrole Containing Small Molecules for Organic Field-Effect Transistors, *ACS Appl. Electron. Mater.*, 2022, **4**(11), 5340–5350, DOI: 10.1021/acsaelm.2c01033.

19 B. Lim, H. Sun, J. Lee and Y.-Y. Noh, High Performance Solution Processed Organic Field Effect Transistors with Novel Diketopyrrolopyrrole-Containing Small Molecules, *Sci. Rep.*, 2017, **7**(1), 164, DOI: 10.1038/s41598-017-00277-7.

20 M. C. Vebber, T. M. Grant, J. L. Brusso and B. H. Lessard, Bis(Trialkylsilyl Oxide) Silicon Phthalocyanines: Understanding the Role of Solubility in Device Performance as Ternary Additives in Organic Photovoltaics, *Langmuir*, 2020, **36**(10), 2612–2621, DOI: 10.1021/acs.langmuir.9b03772.

21 R. R. Cranston, M. C. Vebber, J. F. Berbigier, N. A. Rice, C. Tonnelé, Z. J. Comeau, N. T. Boileau, J. L. Brusso, A. J. Shuhendler, F. Castet, L. Muccioli, T. L. Kelly and

B. H. Lessard, Thin-Film Engineering of Solution-Processable n-Type Silicon Phthalocyanines for Organic Thin-Film Transistors, *ACS Appl. Mater. Interfaces*, 2021, **13**(1), 1008–1020, DOI: **10.1021/acsami.0c17657**.

22 B. King, O. A. Melville, N. A. Rice, S. Kashani, C. Tonnelé, H. Raboui, S. Swaraj, T. M. Grant, T. McAfee, T. P. Bender, H. Ade, F. Castet, L. Muccioli and B. H. Lessard, Silicon Phthalocyanines for N-Type Organic Thin-Film Transistors: Development of Structure–Property Relationships, *ACS Appl. Electron. Mater.*, 2021, **3**(1), 325–336, DOI: **10.1021/acsaelm.0c00871**.

23 B. King, A. J. Daszczynski, N. A. Rice, A. J. Peltekoff, N. J. Yutronkie, B. H. Lessard and J. L. Brusso, Cyanophenoxy-Substituted Silicon Phthalocyanines for Low Threshold Voltage n-Type Organic Thin-Film Transistors, *ACS Appl. Electron. Mater.*, 2021, **3**(5), 2212–2223, DOI: **10.1021/acsaelm.1c00175**.

24 B. H. Lessard, The Rise of Silicon Phthalocyanine: From Organic Photovoltaics to Organic Thin Film Transistors, *ACS Appl. Mater. Interfaces*, 2021, **13**(27), 31321–31330, DOI: **10.1021/acsami.1c06060**.

25 O. A. Melville, T. M. Grant, K. Lochhead, B. King, R. Ambrose, N. A. Rice, N. T. Boileau, A. J. Peltekoff, M. Tousignant, I. G. Hill and B. H. Lessard, Contact Engineering Using Manganese, Chromium, and Bathocuproine in Group 14 Phthalocyanine Organic Thin-Film Transistors, *ACS Appl. Electron. Mater.*, 2020, **2**(5), 1313–1322, DOI: **10.1021/acsaelm.0c00104**.

26 B. King, C. L. Radford, M. C. Vebber, B. Ronnasi and B. H. Lessard, Not Just Surface Energy: The Role of Bis(Pentafluorophenoxy) Silicon Phthalocyanine Axial Functionalization and Molecular Orientation on Organic Thin-Film Transistor Performance, *ACS Appl. Mater. Interfaces*, 2023, **15**(11), 14937–14947, DOI: **10.1021/acsami.2c22789**.

27 R. B. Ewenike, B. King, A. M. Battaglia, J. D. Quezada Borja, Z. S. Lin, J. G. Manion, J. L. Brusso, T. L. Kelly, D. S. Seferos and B. H. Lessard, Toward Weak Epitaxial Growth of Silicon Phthalocyanines: How the Choice of the Optimal Templating Layer Differs from Traditional Phthalocyanines, *ACS Appl. Electron. Mater.*, 2023, **5**(12), 7023–7033, DOI: **10.1021/acsaelm.3c01389**.

28 R. R. Cranston, M. C. Vebber, J. Faleiro Berbigier, J. Brusso, T. L. Kelly and B. H. Lessard, High Performance Solution Processed N-Type OTFTs through Surface Engineered F–F Interactions Using Asymmetric Silicon Phthalocyanines, *Adv. Electron. Mater.*, 2022, **8**(12), 2200696, DOI: **10.1002/aelm.202200696**.

29 R. B. Ewenike, Z. S. Lin, R. R. Cranston, H. R. Lamontagne, A. J. Shuhendler, C.-H. Kim, J. L. Brusso and B. H. Lessard, Engineering the Template Layer for Silicon Phthalocyanine-Based Organic Thin Film Transistors, *Adv. Funct. Mater.*, 2024, **34**(48), 2408779, DOI: **10.1002/adfm.202408779**.

30 B. Ronnasi, B. King, S. Brixi, S. Swaraj, J. Niskanen and B. H. Lessard, Electron Donating Functional Polymer Dielectrics to Reduce the Threshold Voltage of N-Type Organic Thin-Film Transistors, *Adv. Electron. Mater.*, 2024, **10**(8), 2300810, DOI: **10.1002/aelm.202300810**.

31 R. R. Cranston, T. D. Lanosky, R. Ewenike, S. Mckillop, B. King and B. H. Lessard, Polarized Raman Microscopy to Image Microstructure Changes in Silicon Phthalocyanine Thin-Films, *Small Sci.*, 2024, **4**(6), 2300350, DOI: **10.1002/smsc.202300350**.

32 R. R. Cranston, B. King, C. Dindault, T. M. Grant, N. A. Rice, C. Tonnelé, L. Muccioli, F. Castet, S. Swaraj and B. H. Lessard, Highlighting the Processing Versatility of a Silicon Phthalocyanine Derivative for Organic Thin-Film Transistors, *J. Mater. Chem. C*, 2022, **10**(2), 485–495, DOI: **10.1039/D1TC05238A**.

33 B. King, M. C. Vebber, R. Ewenike, M. Dupuy, C. French, J. L. Brusso and B. H. Lessard, Peripherally Fluorinated Silicon Phthalocyanines: How Many Fluorine Groups Are Necessary for Air-Stable Electron Transport in Organic Thin-Film Transistors, *Chem. Mater.*, 2023, **35**(20), 8517–8528, DOI: **10.1021/acs.chemmater.3c01342**.

34 M. C. Vebber, B. King, C. French, M. Tousignant, B. Ronnasi, C. Dindault, G. Wantz, L. Hirsch, J. Brusso and B. H. Lessard, From P-Type to N-Type: Peripheral Fluorination of Axially Substituted Silicon Phthalocyanines Enables Fine Tuning of Charge Transport, *Can. J. Chem. Eng.*, 2023, **101**(6), 3019–3031, DOI: **10.1002/cjce.24843**.

35 N. Ledos, H. R. Lamontagne, J. Manion, F. Castet, B. H. Lessard and J. L. Brusso, Siloxane-Functionalized Silicon Phthalocyanine OTFTs: High Hole Mobility and Unexpected p-Type Character, *Adv. Funct. Mater.*, 2025, e14609, DOI: **10.1002/adfm.202514609**.

36 M. K. Lowery, A. J. Starshak, J. N. Esposito, P. C. Krueger and M. E. Kenney, Dichloro(Phthalocyanino)Silicon, *Inorg. Chem.*, 1965, **4**(1), 128, DOI: **10.1021/ic50023a036**.

37 N. S. Sarai, T. J. Fulton, R. L. O'Meara, K. E. Johnston, S. Brinkmann-Chen, R. R. Maar, R. E. Tecklenburg, J. M. Roberts, J. C. T. Reddel, D. E. Katsoulis and F. H. Arnold, Directed Evolution of Enzymatic Silicon-Carbon Bond Cleavage in Siloxanes, *Science*, 2024, **383**(6681), 438–443, DOI: **10.1126/science.adi5554**.

38 K. Fuchise, T. Kobayashi, K. Sato and M. Igarashi, Organocatalytic Ring-Opening Polymerization of Cyclotrisiloxanes Using Silanols as Initiators for the Precise Synthesis of Asymmetric Linear Polysiloxanes, *Polym. Chem.*, 2020, **11**(48), 7625–7636, DOI: **10.1039/D0PY01251C**.

39 J. Manion and B. H. Lessard, High-Throughput Characterization Is Key to Report Reliable Organic Thin-Film Transistor Performance, *Nat. Rev. Mater.*, 2024, **9**(6), 377–378, DOI: **10.1038/s41578-024-00689-8**.

40 N. Dallaire, N. T. Boileau, I. Myers, S. Brixi, M. Ourabi, E. Raluchukwu, R. Cranston, H. R. Lamontagne, B. King, B. Ronnasi, O. A. Melville, J. G. Manion and B. H. Lessard, High Throughput Characterization of Organic Thin Film Transistors, *Adv. Mater.*, 2024, **36**(44), 2406105, DOI: **10.1002/adma.202406105**.

41 Y. Yang, B. Samas, V. O. Kennedy, D. Macikenas, B. L. Chaloux, J. A. Miller, R. L. Speer, J. Protasiewicz, A. A. Pinkerton and M. E. Kenney, Long, Directional Interactions in Cofacial Silicon Phthalocyanine Oligomers, *J. Phys. Chem. A*, 2011, **115**(45), 12474–12485, DOI: **10.1021/jp2019445**.

42 J. Rivnay, S. C. B. Mannsfeld, C. E. Miller, A. Salleo and M. F. Toney, Quantitative Determination of Organic Semiconductor Microstructure from the Molecular to Device Scale, *Chem. Rev.*, 2012, **112**(10), 5488–5519, DOI: **10.1021/cr3001109**.

43 (*a*) CCDC 2487841: Experimental Crystal Structure Determination, 2025, DOI: **10.5517/ccdc.csd.cc2phsyy**; (*b*) CCDC 2487842: Experimental Crystal Structure Determination, 2025, DOI: **10.5517/ccdc.csd.cc2phszz**; (*c*) CCDC 2487844: Experimental Crystal Structure Determination, 2025, DOI: **10.5517/ccdc.csd.cc2pht12**; (*d*) CCDC 2487846: Experimental Crystal Structure Determination, 2025, DOI: **10.5517/ccdc.csd.cc2pht34**.

Volume 10 | Number 1 | 5 January 2026

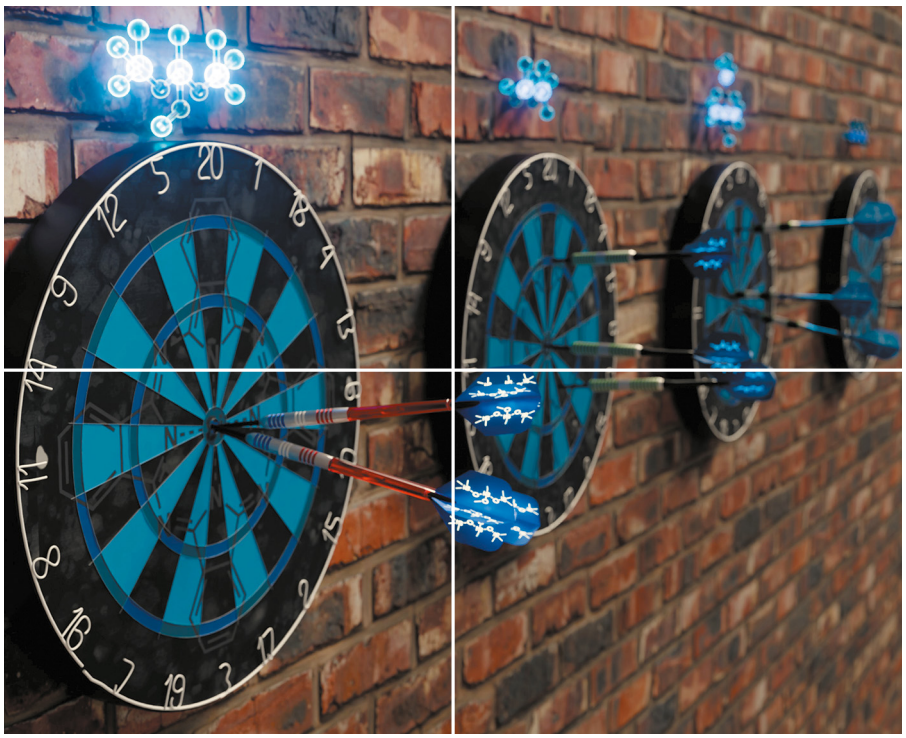

MATERIALS CHEMISTRY

FRONTIERS

CCS 中国化学会 CHINESE CHEMICAL SOCIETY
ICCAS 1956 中国科学院化学研究所 CHINESE ACADEMY OF CHEMISTRY
ROYAL SOCIETY OF CHEMISTRY
rsc.li/frontiers-materials